Supporting Information

Inter-chain Double-site Synergetic Photocatalytic Hydrogen Evolution in Robust Cuprous Coordination Polymer

Ying Zang,[‡a] Jiangwei Zhang,[‡c] Rui Wang,[a] Zhao-Di Wang,[a] Yandi Zhu,[b] Xiaoyan Ren,[b] Shunfang Li,[*b] Xi-Yan Dong,[d] Shuang-Quan Zang[*a]

[a]Green Catalysis Center, and College of Chemistry, Zhengzhou University, Zhengzhou 450001 (China)

[b]School of Physics and Microelectronics, Zhengzhou University, Zhengzhou 450001 (China)

[c]State Key Laboratory of Catalysis, Dalian Institute of Chemical Physics, Chinese Academy of Sciences (CAS) Dalian 116023, P. R. China

[d]College of Chemistry and Chemical Engineering, Henan Polytechnic University, Jiaozuo 454000, China

E-mail: zangsqzg@zzu.edu.cn

E-mail: sflizzu@zzu.edu.cn

Table of Contents

Experimental section

Materials and reagents. All chemicals were purchased through commercial suppliers and used without further purification.

Instrumentation. The XRD patterns were recorded on a Rigaku MiniFlex 600 diffractometer at 30 kV, and Cu-Kα (λ = 1.5418 Å) at ambient temperature. Photoluminescence spectra were determined by a Horiba Scientific FluoroMax-4 spectrofluorometer spectrometer. Thermogravimetric (TG) analyses were performed on a SDT 2960 thermal analyzer from room temperature to 900 °C at a heating rate of 5 °C min^{-1} under nitrogen atmosphere. Fourier transform infrared (FT-IR) spectra were recorded on a Bruker TENSOR 27 FT-IR spectrometer in the 400-4000 cm^{-1} region with KBr pellets. Elemental analyses (EA) were carried out with a Perkin-Elmer 240 elemental analyser. Cyclic voltammetry (CV) measurements of Cu-MIM and the bare glassy carbon (GC) electrode were performed with CHI 660E in aqueous KOH solution at pH = 11. Conditions: glassy carbon as working electrode, Pt plate as counter electrode, and Ag/AgCl as reference electrode, scan rate: 100 mV s^{-1} at room temperature. Working electrode preparation: the object samples were dispersed in water by ultrasonication for 20 minutes, dripped on glassy carbon (GC) electrode (S = 0.07 cm^2), and then dried in the air.

XAFS measurements: The X-ray absorption find structure spectra (Cu K-edge) were collected at 1W1B beamline of Beijing Synchrotron Radiation Facility (BSRF). The data were collected in transmission mode using a Lytle detector. The samples were grinded and uniformly daubed on the special adhesive tape.

XAFS Analysis and Results: The acquired EXAFS data were processed according to the standard procedures using the ATHENA module of Demeter software packages. The EXAFS spectra were obtained by subtracting the post-edge background from the overall absorption and then normalizing with respect to the edge-jump step. Subsequently, the χ(k) data of were Fourier transformed to real (R) space using a hanning windows (dk=1.0 $Å^{-1}$) to separate the EXAFS contributions from different coordination shells. To obtain the quantitative structural parameters around central atoms, least-squares curve parameter fitting was performed using the ARTEMIS module of Demeter software packages.

The following EXAFS equation was used:

$$\chi(k) = \sum_j \frac{N_j S_o^2 F_j(k)}{kR_i^2} \cdot \exp[-2k^2\sigma_j^2] \cdot \exp[\frac{-2R_j}{\lambda(k)}] \cdot \sin[2kR_j + \phi_j(k)]$$

the theoretical scattering amplitudes, phase shifts and the photoelectron mean free path for all paths calculated. S_{02} is the amplitude reduction factor, $F_j(k)$ is the effective curved-wave backscattering amplitude, N_j is the number of neighbors in the jth atomic shell, R_j is the distance between the Xray absorbing central atom and the atoms in the j^{th} atomic shell (backscatterer), λ is the mean free path in Å, $\phi_j(k)$ is the phase shift (including the phase shift for each shell and the total central atom phase shift), σ_j is the Debye-Waller parameter of the j^{th} atomic shell (variation of distances around the average R_j). The functions $F_j(k)$, λ and $\phi_j(k)$ were calculated with the ab initio code $FEFF_9$. The additional details for EXAFS simulations are given below.

All fits were performed in the *R* space with *k*-weight of 2. The coordination numbers of model samples were fixed as the nominal values. The obtained S_{02} was fixed in the subsequent

fitting. While the internal atomic distances R, Debye-Waller factor σ^2, and the edge-energy shift Δ were allowed to run freely.

Photocatalytic Hydrogen Generation Experiments. Photocatalytic reaction was conducted in a 70 mL Pyrex cell with the visible-light. In a typical photocatalytic experiment, the catalyst (1.0 mg) was suspended in H_2O/MeOH (v:v = 1:2) containing TEA (2 mL) and EY (7.0 mg). Before irradiation, the suspension of the catalyst was dispersed in an ultrasonic bath for 10 minutes, and then N_2 was bubbled through the reaction mixture for 20 minutes to completely remove oxygen. Sampling was conducted intermittently through the silicone rubber septum during experiments. The amount of produced H_2 was monitored in real time by GC analysis of the headspace gases by using an Agilent GC7820 Gas Chromatograph (N_2 as gas carrier).

General procedures

Synthesis of Cu-MIM. A solution of $Cu(NO_3)_2{\cdot}3H_2O$ (0.242 g, 1.0 mmol), 2-methylimidazole (MIM) (0.081 g,1.0 mmol), and aqueous ammonia (25%, 5 mL), was stirred for 15 min in air, then transferred and sealed in a 10 mL Teflon-lined vessel, the solvothermal reaction was going on 80 h under 160 °C, after cooling to room temperature, the resulting crystals were filtered, washed by methanol, and dried under Ar.[1] (EA calcd(%) for $C_4H_5CuN_2$: C 33.22, H 3.48, N 19.37; found: C 32.89, H 3.52, N 19.13).

Synthesis of Cu-EIM. A solution of $Cu(NO_3)_2{\cdot}3H_2O$ (0.242 g, 1.0 mmol), 2-ethylimidazole (EIM) (0.095 g, 1.0 mmol), aqueous ammonia (25%, 5 mL) and cyclohexane (3 mL) was stirred for 15 min in air, then transferred and sealed in a 10 mL Teflon-lined vessel, the solvothermal reaction was going on 80 h under 160 °C, after cooling to room temperature, the resulting pale yellow needle crystals were filtered, washed, and dried under Ar.[2] (EA calcd(%) for $C_5H_7CuN_2$: C 37.85, H 4.45, N 17.66; found: C 37.56, H 4.21, N 17.41).

Synthesis of Cu-IPIM. A solution of $Cu(NO_3)_2{\cdot}3H_2O$ (0.242 g, 1.0 mmol), 2-isopropylimidazole (IPIM) (0.081 g, 1.0 mmol), and aqueous ammonia (25%, 6 mL), was stirred for 15 min in air, then transferred and sealed in a 10 mL Teflon-lined vessel, the solvothermal reaction was going on 80 h under 160 °C, after cooling to room temperature, the resulting crystals were filtered, washed by methanol, and dried under Ar.[3] (EA calcd (%) for $C_6H_9CuN_2$: C 41.73; H 5.22; N 16.23. Found: C 41.64; H 5.23; N 16.09).

Calculation details.

Our spin-polarized DFT calculations[4] are carried out using the Vienna ab-initio simulation package (VASP)[5] with projector-augmented wave (PAW) method[6] and the Perdew Burke and Ernzerhof (PBE)[7] as parametrized by Perdew and Zunger for the exchange-correlation functional. The three catalysts of Cu-MIM, Cu-EIM, and Cu-IPIM systems are briefly simulated by one-dimensional (1D) single- and double-chain models consisting of –[Cu-imidazole-Cu]– periodic units, see Figure S16. A vacuum region of 15 Å thickness is used to ensure the decoupling between the neighbouring images. During the structural relaxation, all atoms are fully relaxed until the residual forces on each direction are smaller than 0.02 eV/Å. A 3 × 1 × 1 k-point mesh was used for the 1 × 1 × 1 supercell of all the three systems. The energy cutoff is set to 400 eV in all the calculations. The average binding energy of a H atom on the catalyst substrate is defined as $E_b = -[E(n\text{H/Catalyst}) - E(\text{Catalyst}) - nE(H_{atom})]/n$. In right side of the formula, the first three terms represent the total energies of the optimize *n*H/catalyst complex, the optimized catalyst substrate, the energy of a H atom in the gas phase, respectively, and *n* is the total number of the adsorbed H atom. To investigate the

kinetic processes of the H_2 generation, the improved climbing-image nudged elastic band (cNEB) method[8, 9] is used to identify the transition states (TS) and minimum energy paths (MEP).

Supplementary Figures

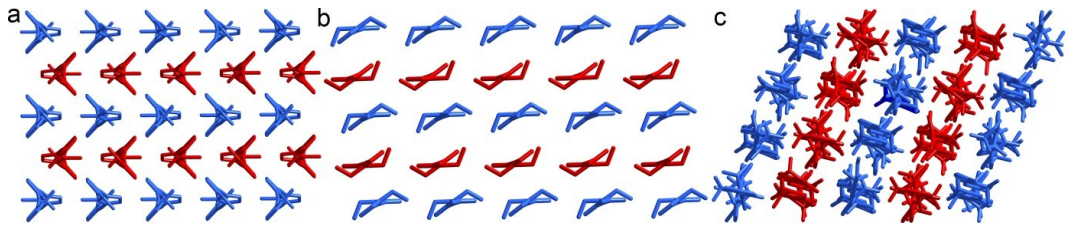

Figure S1. The crystal packing diagram and one-dimensional chain structure of Cu-MIM (a), Cu-EIM (b) and Cu-IPIM (c) respectively.

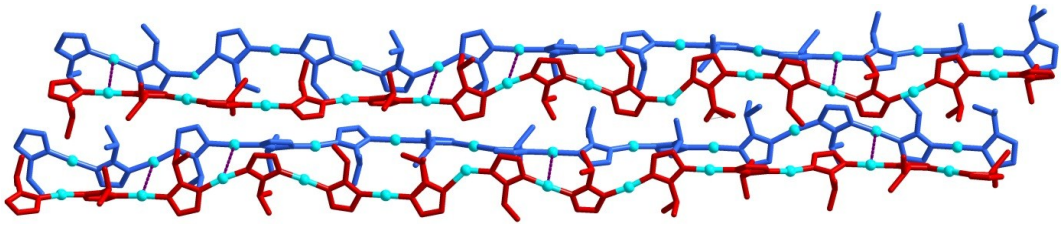

Figure S2. The shortest distance (purple line) of copper to copper between the adjacent chain of Cu-IPIM.

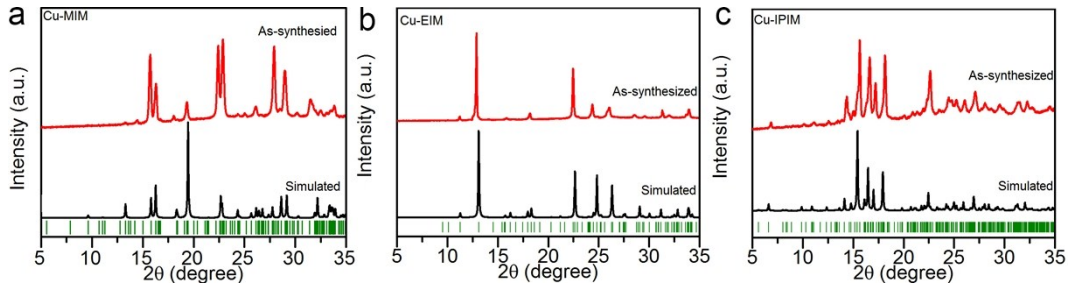

Figure S3. PXRD patterns of Cu-MIM (a), Cu-EIM (b) and Cu-IPIM (c).

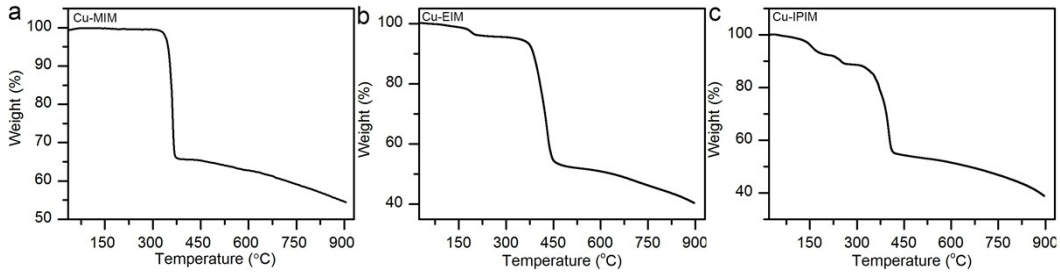

Figure S4. TG curves of Cu-MIM (a), Cu-EIM (b) and Cu-IPIM (c).

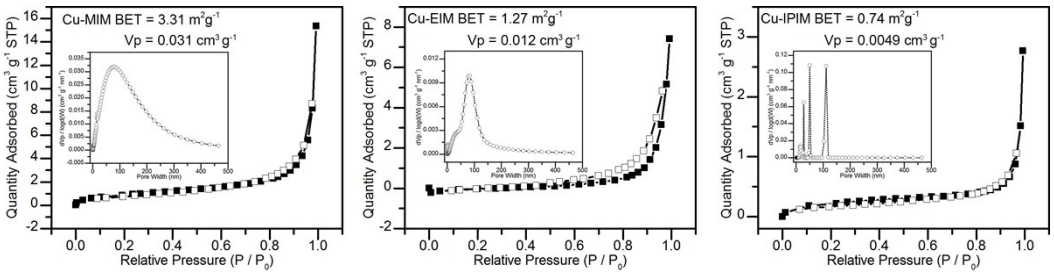

Figure S5. Nitrogen sorption isotherms for Cu-MIM, Cu-EIM and Cu-IPIM, the inset shows the pore size distributions of Cu-MIM, Cu-EIM and Cu-IPIM respectively.

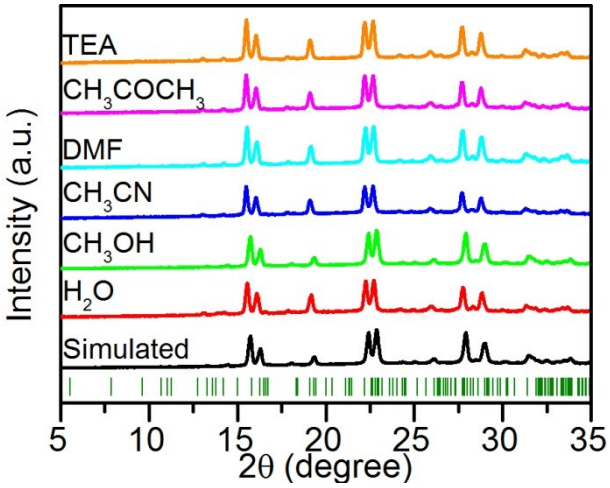

Figure S6. PXRD patterns of Cu-MIM (simulated, immersed in some common organic solvents for 24 hours).

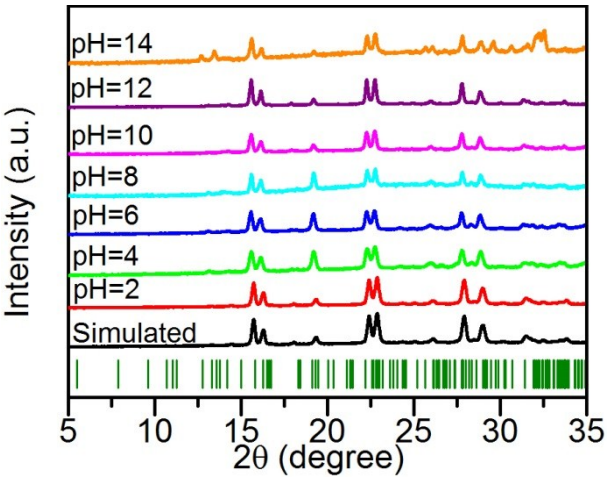

Figure S7. PXRD patterns of Cu-MIM (simulated, treated with different pH for 24 hours).

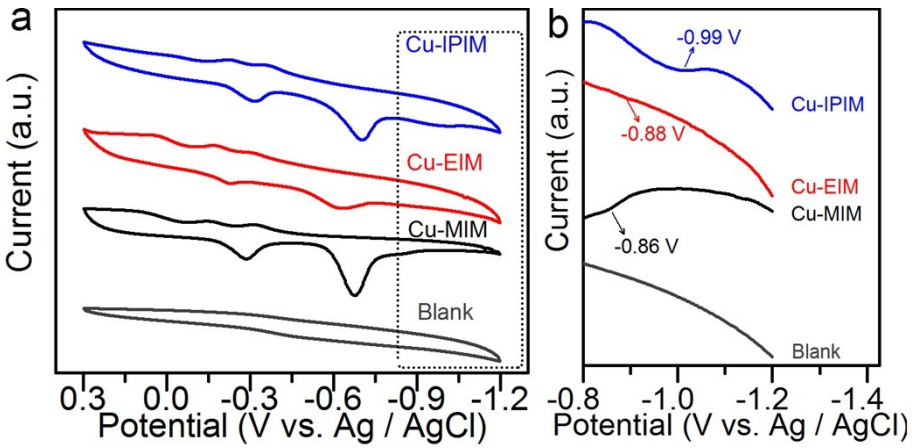

Figure S8. CV curves of Cu-MIM, Cu-EIM and Cu-IPIM (in aqueous KOH solution at pH = 11).

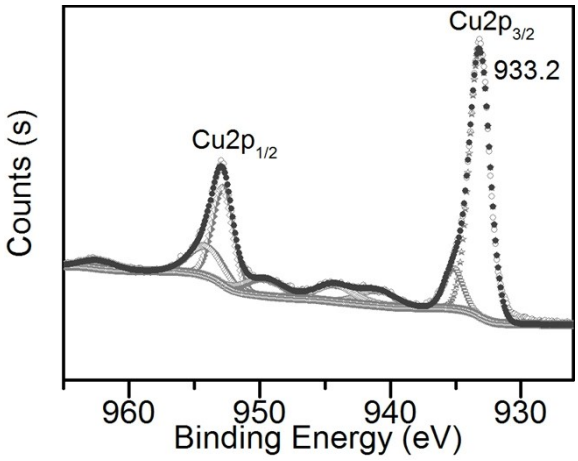

Figure S9. High-resolution XPS spectrum of Cu 2p for of Cu-MIM.

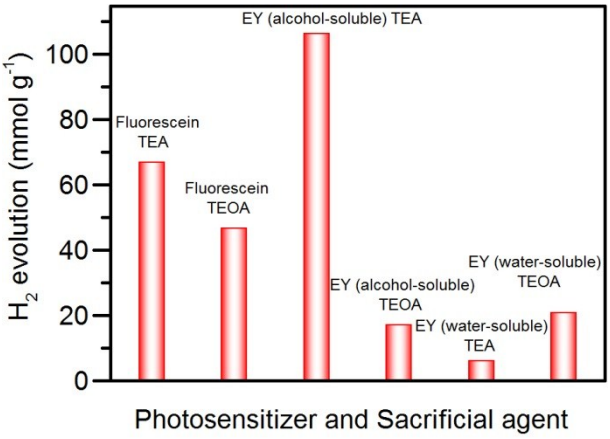

Figure S10. The effect of photosensitizer and sacrificial agent on H_2 evolution. H_2 evolution condition: MeOH/H_2O (1:1) in the presence of 2 mg of Cu-MIM in 30 mL solution containing sacrificial agent (2 mL) and 5 mg of photosensitizer under an inert atmosphere. The system was irradiated with a visible-light.

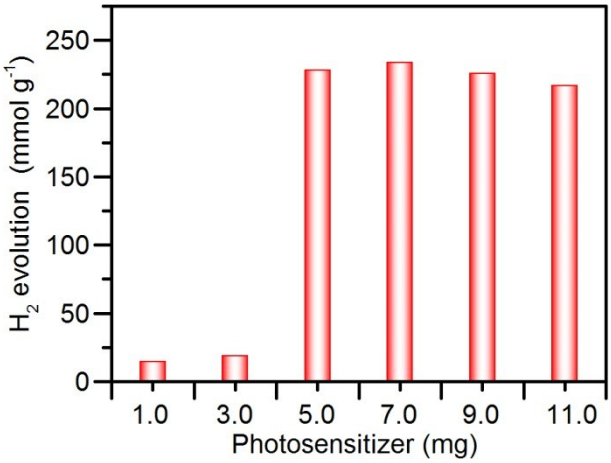

Figure S11. The effect of the different mass of photosensitizer on H_2 evolution. H_2 evolution condition: MeOH/H_2O (1:1) in the presence of 2 mg of Cu-MIM in 30 mL solution containing TEA (2 mL) under an inert atmosphere. The system was irradiated with a visible-light.

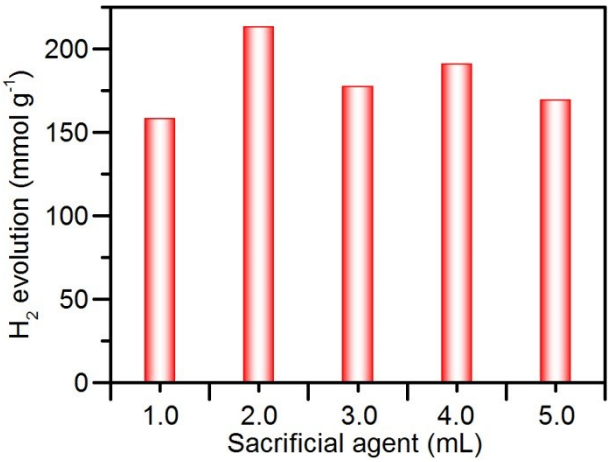

Figure S12. The effect of the volume of sacrificial agent on H_2 evolution. H_2 evolution condition: MeOH/H_2O (1:1) in the presence of 2 mg of Cu-MIM and 7 mg of EY (alcohol-soluble) under an inert atmosphere. The system was irradiated with a visible-light.

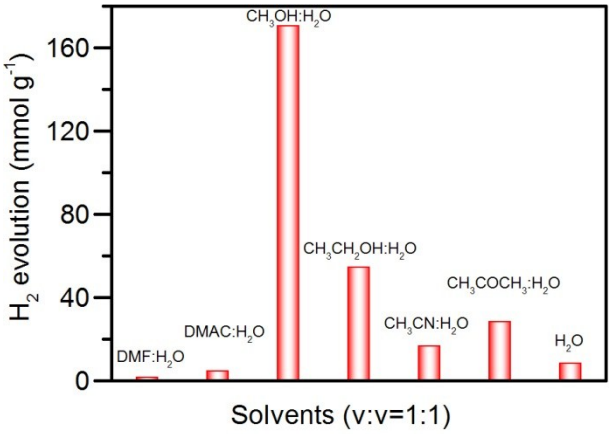

Figure S13. The effect of solvents on H_2 evolution. H_2 evolution condition: 2 mg of Cu-MIM in 30 mL solution containing TEA (2 mL) and 7 mg of EY (alcohol-soluble) under an inert atmosphere. The system was irradiated with a visible-light.

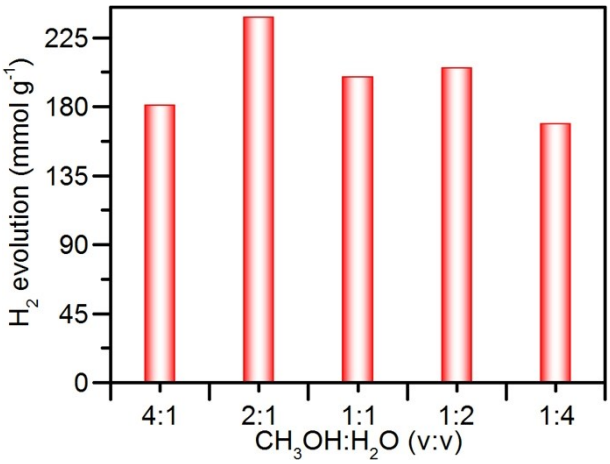

Figure S14. The effect of the solvents ratio on H_2 evolution. H_2 evolution condition: 2 mg of Cu-MIM in 30 mL solution containing TEA (2 mL) and 7 mg of EY (alcohol-soluble) under an inert atmosphere. The system was irradiated with a visible-light.

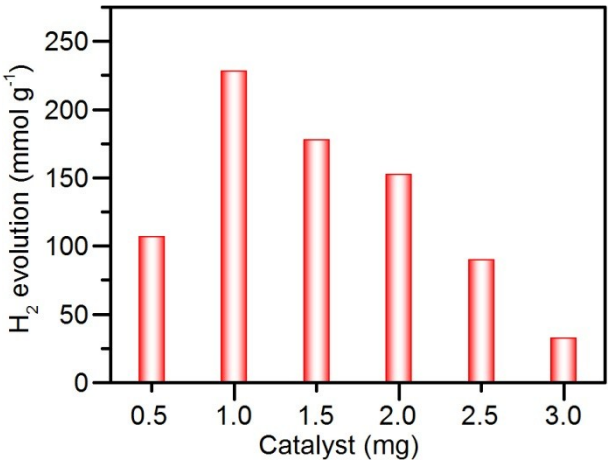

Figure S15. The effect of the different mass of catalyst on H_2 evolution. H_2 evolution condition: MeOH/H_2O (2:1) in the presence of 7 mg of EY (alcohol-soluble) in 30 mL solution containing TEA (2 mL) under an inert atmosphere. The system was irradiated with a visible-light.

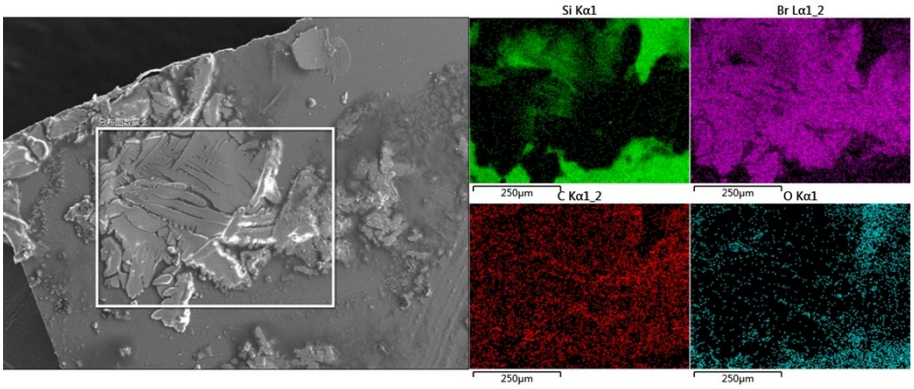

Figure S16. Energy dispersive spectroscopy (EDS) mapping results of the solution after 6 cycles. (The sample was prepared on the slicion slice, Br comes from EY).

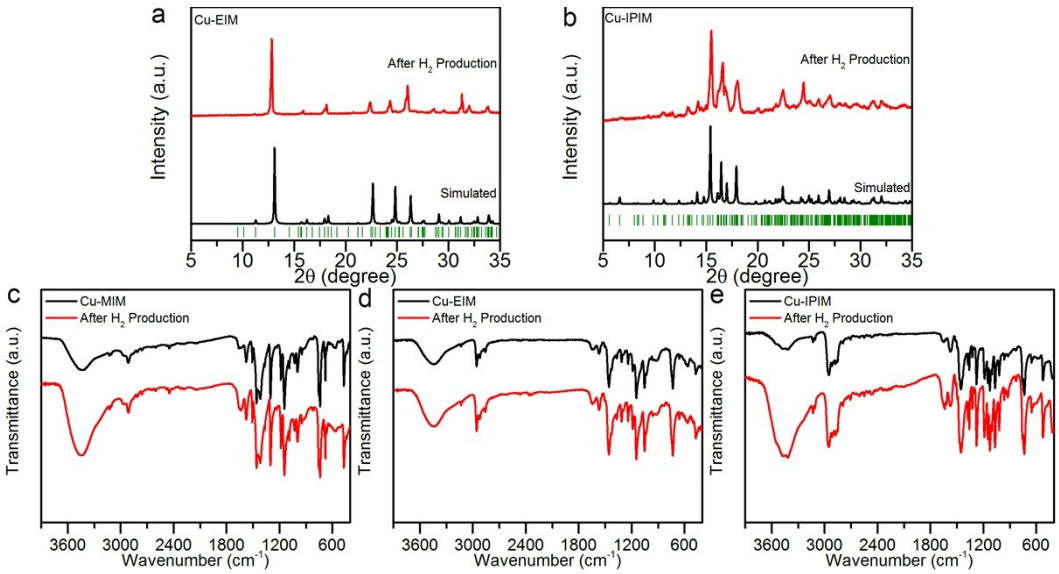

Figure S17. PXRD patterns of Cu-EIM (a) and Cu-IPIM (b) after photocatalytic reaction, IR of Cu-MIM (c), Cu-EIM (d) and Cu-IPIM (e) before and after H_2 production.

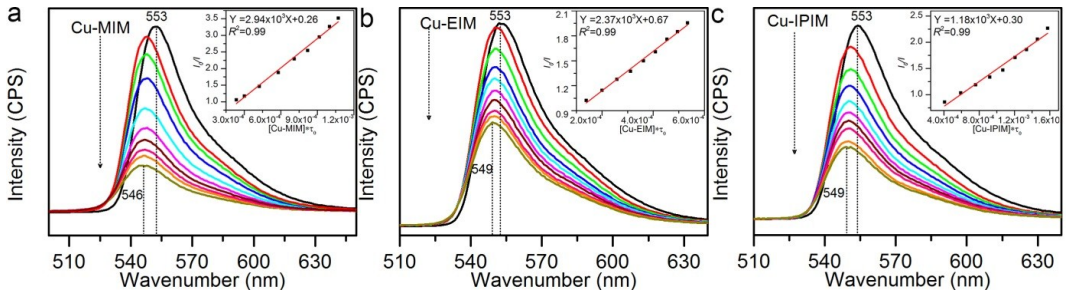

Figure S18. Emission spectra of EY as a function of Cu-MIM (a), Cu-EIM (b). Cu-IPIM (c). Inset: Stern-Volmer plot for the photoluminescence quenching of EY.

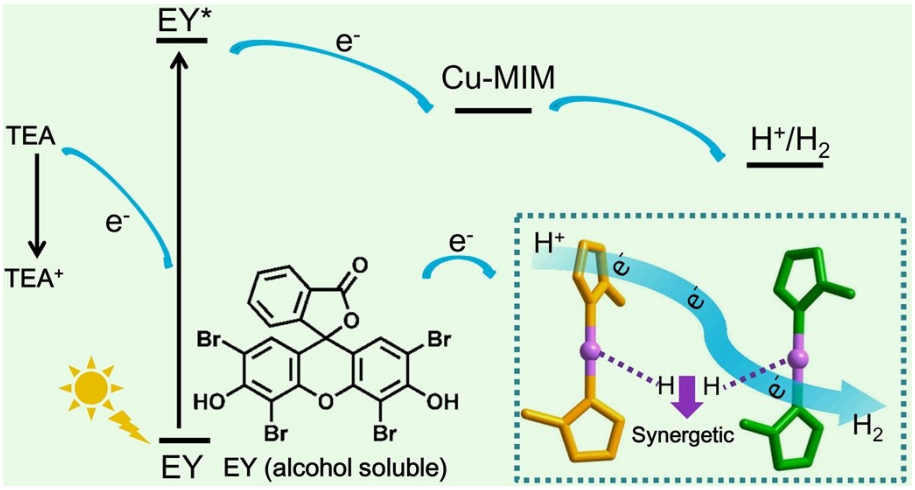

Figure S19. Reaction scheme for the generation of H_2 under visible-light irradiation.

Based on these experimental results, we proposed the electron transfer pathways involved in photo-induced hydrogen production in the system (Figure S19). First, the photosensitizer EY are excited by the visible light, then the photoelectrons are transferred from the excited-state EY* to the catalyst (Cu-MIM). Subsequently, the protons were reduced by the photoelectrons at the surface of catalyst where the synergism of dual-copper sites prompts the generation of dihydrogen, as addressed later. Meanwhile, the sacrificial agent (TEA) consumed the photo-generated holes recover the photosensitizer.

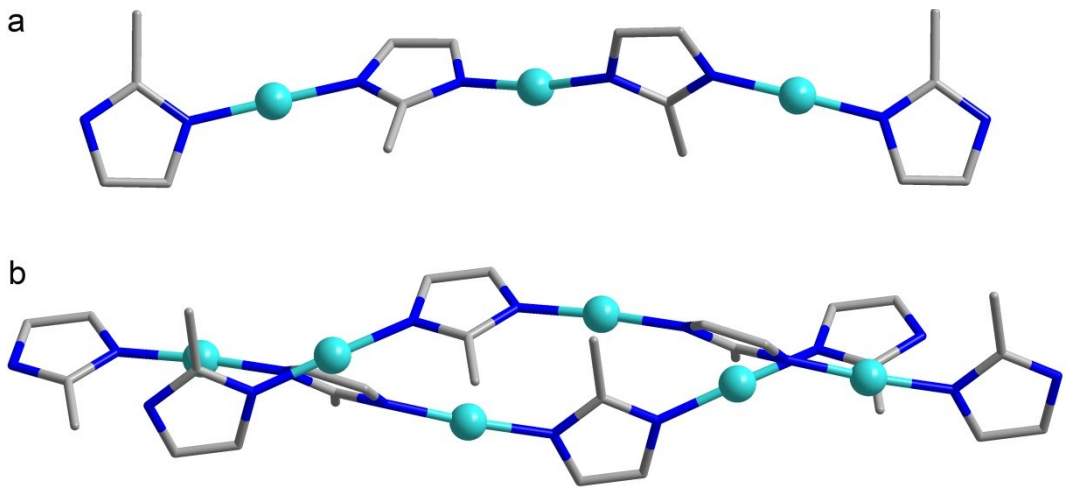

Figure S20. (a)1D chain model of Cu-MIM. (b) Double-chain model of Cu-MIM.

The first model is single-chain structures constructed by periodic –Cu–imidazole(R)–Cu– units (Figure S20a); the second model, which contains two adjacent chains adapted from single crystal data (Figure S20b).

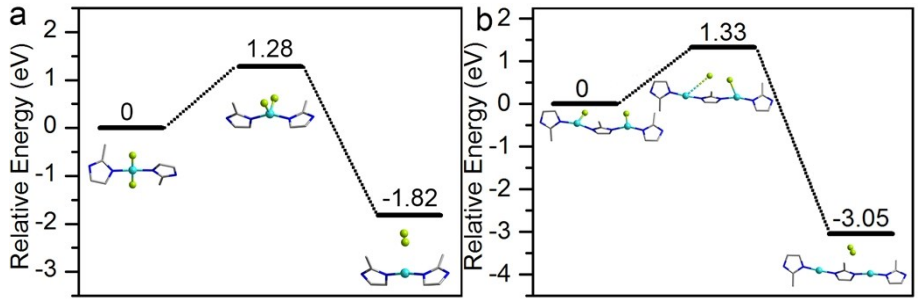

Figure S21. Potential barrier of Cu-MIM based on a 1D chain with reaction mechanism of M-I (a) or M-II (b).

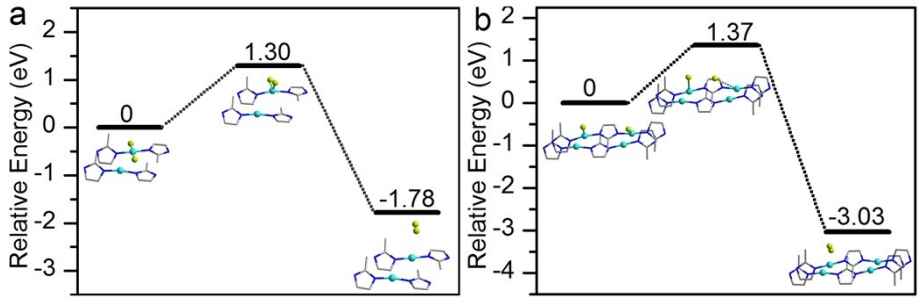

Figure S22. Potential barrier of Cu-MIM based on two neighbouring 1D chains with reaction mechanism of M-I (a) or M-II (b).

NOTE: In this case, three possible ways for H atoms adsorbed on Cu active sits are examined. For the first way similar to M-I, two H atoms adsorb on the same Cu site in one of the double chains, where the H_2 evolution energy barrier of Cu-MIM is still high up to 1.30 eV (Figure S22a), similar to that in single-chain M-I

mechanism; for the second way similar to M-II in the single-chain mode, two H atoms adsorb on the two neighboring Cu sites in one of the double chains, a similarly high energy barrier of 1.37 eV for Cu-MIM is observed (Figure S22b). Subsequently, we turn to the third way, on which two H atoms could be adsorbed on the two adjacent Cu sites separately located on two neighboring chains. The difference among these three cases is that, two H atoms can immediately bind to form H_2 after desorption from Cu sites in Cu-MIM, due to the shortest inter-chain separation; while for Cu-EIM and Cu-IPIM, H atoms adsorbed on the Cu sites are transferred by the aid of imidazole (R) before they bond together to form dihydrogen, due to the larger inter-chain separation (Figure S23).

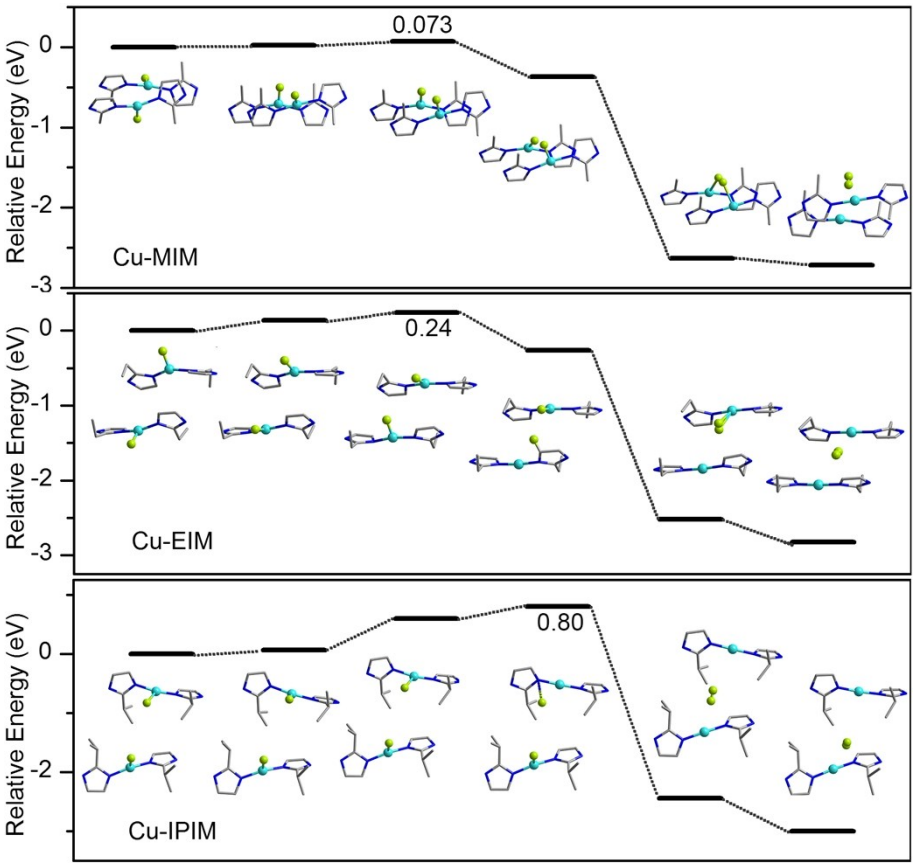

Figure S23. Hydrogen evolution processes with the SC mechanism of Cu-MIM (a), Cu-EIM (b) and Cu-IPIM (c). In (a), the H_2 is formed via a direct H-H combination mechanism with the two adsorbed H atom smoothly rotating around each Cu site; in (b) and (c), due to the relatively larger inter-chain separations (see also Figure S25), the two H atoms combined together via one H atom translated along the ligands, as indicated by the dashed lines in (b) and (c).

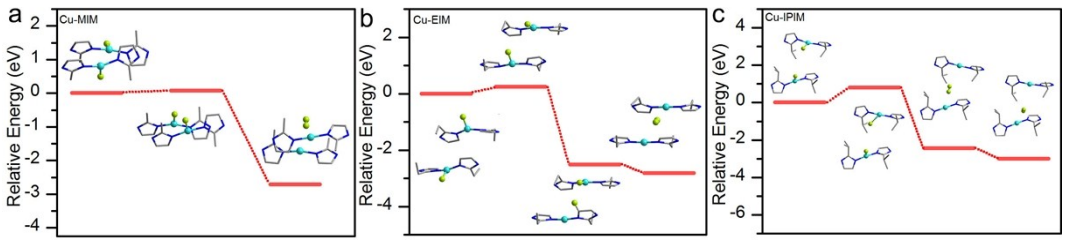

Figure S24. The increased E_{bar} for the latter two cases are due to the weakened inter-chain cooperative catalysis.

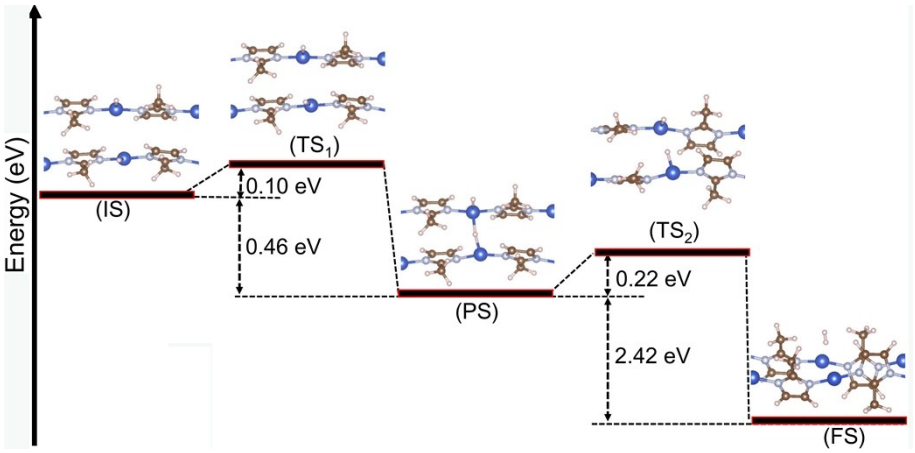

Figure S25. The optimized minimum energy path for H_2 generation via the established inter-chain double-site synergetic mechanism occurred on the surface of Cu-MIM crystal.

Table S1. Photocatalytic H_2-production performance for catalysts in the literatures. This table consists of three sections. Section 1: Single atom/site @ inorganic supports; Section 2: Single atom/site @ MOF/COF supports; Section 3: Metal particles @ MOF/COF supports; Section 4: MOFs for photocatalytic H_2 production including three complexes in this work.

Section 1: Single atom/site @ inorganic supports for photocatalytic H_2 production				
Single atom/site @ support	Single atom/site	Matrix/Linker	Activity	Reference
Pt_1@def-TiO_2[S10]	Pt	def-TiO_2	~5.5 mmol·g^{-1}·h^{-1}	*Angew. Chem. Int. Ed.* **2020**, 59 (3), 1295-1301
Cu@TiO_2[S11]	Cu	TiO_2	16 mmol·g^{-1}·h^{-1}	*Nat. Mater.* **2019**, 18 (6), 620-628
Co-N-C[S12]	Co	HAT-6CN	1.18 mmol·g^{-1}·h^{-1}	*Chem. Sci.* **2019**, *10 (9),* 2585-2591
Fe@g-C_3N_4[S13]	Fe	g-C_3N_4	3.39 mmol·g^{-1}·h^{-1}	*Small.* **2019**, 15 (50),
CNUHAu[S14]	Au	g-C_3N_4	~0.016 mmol·g^{-1}·h^{-1}	*J. Mater. Chem. A.* **2019**, 7 (42), 24217-24211
CdS@CDs/ PtSAs[S15]	Pt	Carbon dots decorated ultrathin CdS nanosheets	45.5 mmol·g^{-1}·h^{-1}	*Applied Catalysis B: Environmental.* **2019**, 259 (15), 118036
HNTM-IrPt[S16]	Ir and Pt	zirconium–porphyrinic MOF	~0.21 mmol·g^{-1}·h^{-1}	*Angew. Chem. Int. Ed.* **2018**, 57 (13), 3493-3498.
Ni-NG/CdS[S17]	Pt	Nitrogen-Doped Graphene	270.22 mmol·g^{-1}·h^{-1}	*ACS Catal.* **2018**, 8 (12), 11863-11874
Pd@g-CN[S18]	Pd	graphitic carbon nitride	~6.69 mmol·g^{-1}·h^{-1}	*Adv. Funct. Mater.* **2018**, 28 (32), 1802169
Pt^{II}-C_3N_4[S19]	Pt^{II}	g-C_3N_4	0.14 mmol·g^{-1}·h^{-1}	*J. Phys. Chem. C.* **2018**, 122 (37), 21108-21114
Pt-SACN[S20]	Pt	g-C_3N_4	1.39 mmol·g^{-1}·h^{-1}	*ACS Appl. Energy Mater.* **2018,** 1 (11), 6082-6088
Co_1-P_4@ g-C_3N_4[S21]	Co	g-C_3N_4	~0.41 mmol·g^{-1}·h^{-1}	*Angew. Chem. Int. Ed.* **2017**, 56 (32), 9312-9317
Co_1-N_4[S22]	Co	g-C_3N_4	~0.22 mmol·g^{-1}·h^{-1}	*Angew. Chem. Int. Ed.* **2017**, 56 (40), 12191-12196
Pt_1Ag_{24}/g-C_3N_4[S23]	Pt	g-C_3N_4	1.32 mmol·g^{-1}·h^{-1}	*Chem. Commun.* **2017**, 53 (68), 9402-9405
Co-NG-CdS[S24]	Co	g-C_3N_4	13.82 mmol·g^{-1}·h^{-1}	*ACS Appl. Mater. Interfaces.* **2017**, 9 (49),
0.6Pt_1/TiO_2-A[S25]	Ni	TiO_2	8.45 mmol·g^{-1}·h^{-1}	*J. Catal.* **2017**, *353*, 250-255
Pt-CN[S26]	Pt	g-C_3N_4	6.36 mmol·g^{-1}·h^{-1}	*Adv. Mater.* ***2016***, 28 (12), 2427-2431
Section 2: Single atom/site @ MOF/COF supports for photocatalytic H_2 production				

Single atom/site @ MOF/COF	Single atom/site	Matrix/Linker	Activity	Reference
Pt@Cu-TCPP[S27]	Pt	Pt^{II} tetrakis(4-carboxyphenyl)porphyrin (PtTCPP)	11.32 $mmol \cdot g^{-1} \cdot h^{-1}$	*Angew. Chem. Int. Ed.* ***2019***, 58 (30), 10198-10203
Co@ZF9[S28]	Co	benzimidazole	6.42 $mmol \cdot g^{-1} \cdot h^{-1}$	*Chem. Eur. J.* **2019**, 25 (41), 9670-9677
Pt-SACs/MBT[S29]	Pt	MOF-808-EDTA (MBT)	68.33 $mmol \cdot g^{-1} \cdot h^{-1}$	*J. Catal.* **2019**, *375*, 351-360
Al-TCPP-0.1Pt[S30]	Pt	aluminum-based porphyrinic MOF $(AlOH)_2H_2TCPP$	~0.13 $mmol \cdot g^{-1} \cdot h^{-1}$	*Adv. Mater.* **2018**, 30 (7), 1705112
Co@N_2-COF[S31]	Co	N_2-COF	~0.78 $mmol \cdot g^{-1} \cdot h^{-1}$	*J. Am. Chem. Soc.* **2017**, 139 (45), 16228-16234
Section 3: Metal particles @ MOF/COF supports for photocatalytic H_2 production				
Metal-loaded MOFs	Metal loaded	Linker	Activity	Reference
CdS@2.5NMF[S32]	CdS	1,10-phenanthroline and 4,4′-[illegible]	~4.52 $mmol \cdot g^{-1} \cdot h^{-1}$	*Adv. Energy Mater.* **2019**, 9 (11), 1803402
NH_2-UiO-66/TpPa-1-COF[S33]	Pt	2-aminoterephthalic acid p-phenylenediamine	23.41 $mmol \cdot g^{-1} \cdot h^{-1}$	*Angew. Chem. Int. Ed.* **2018**, 57 (37), 12106-12110
Pt@USTC-8(In)[S34]	Pt	indium(III) hydroxide and H_2TCPP	~0.34 $mmol \cdot g^{-1} \cdot h^{-1}$	*ACS Catal.* **2018**, *8 (5)*, 4583-4590
Pt-Zn_3P_2-CoP[S35]	Pt	2-Methylimidazole	~9.15 $mmol \cdot g^{-1} \cdot h^{-1}$	*Nano Energy.* **2017**, *33*, [illegible]
Calix-3/Pt@ UiO-66-NH_2[S36]	Pt, Calix-3	2-aminoterephthalic acid	~1.53 $mmol \cdot g^{-1} \cdot h^{-1}$	*Appl. Catal. B-Environ.* **2017**, 206 (5), 426-433
{[$Cu^{I}Cu^{II}_2$(DCTP)$_2$] $NO_3 \cdot 1.5DMF$}n[S37]	H_2PtCl_6	4′-(3,5-dicarboxyphenyl)-	~0.032$mmol \cdot g^{-1} \cdot h^{-1}$	*Angew. Chem. Int. Ed.* ***2016***, 55 (16), 4938-4942
Pt@UiO-66-NH_2[S38]	Pt	2-aminoterephthalic acid	~0.26 $mmol \cdot g^{-1} \cdot h^{-1}$	*Angew. Chem. Int. Ed.* ***2016***, 55 (32), 9389-9393
Ni@MOF-5[S39]	Ni	1,4-benzene dicarboxylate	~0.03 $mmol \cdot g^{-1} \cdot h^{-1}$	Appl. *Catal. B-Environ.* **2016**, 190 (5), 12-25
POM@UiO[S40]	$[P_2W_{18}O_{62}]^{6-}$	$[Ru(bpy)_3]^{2+}$-derived dicarboxylate ligand	~0.70 $mmol \cdot g^{-1} \cdot h^{-1}$	*J. Am. Chem. Soc.* **2015**, 137 (9), 3197-3200
Co@NH_2-MIL-125[S41]	Co-dioxime diimine	2-aminoterephthalic acid	~0.35 mmol $g^{-1} \cdot h^{-1}$	*Energy Environ. Sci.* **2015**, 8 (1), 364-375
Ru-Pt@UIO-67[S42]	$Pt(dcbpy)Cl^{2+}$ $[Ru(dcbpy)(bpy)_2]^{2+}$	H_2bptc + $Pt(dcbpy)Cl_2$	~0.38 mmol $g_{Pt}^{-1} \cdot h^{-1}$	*J. Mater. Chem. A.* **2015**, 3 (19), 10386-10394

rGO-PDI-Co[S43]	rGO	perylene tetracarboxylic di(propyl imidazole)	~0.23 mmol·g^{-1}·h^{-1}	*ACS Appl. Mater. Interfaces* **2015**, 7 (1), 880-886
g-C_3N_4@UiO-66[S44]	Pt	terephthalate	~1.4 mmol·g^{-1}·h^{-1}	*Adv. Mater. Interfaces*. **2015**, 2 (10), 1500037
ErB + Pt@UiO-66[S45]	Pt	terephthalate	0.46 mmol·g^{-1}·h^{-1}	*Appl. Catal. B-Environ*. **2015**, 168-169, 572-576
Pt@CdS/UiO-66[S46]	Pt	terephthalate	~0.05 mmol·g^{-1}·h^{-1}	*Appl. Surf. Sci*. **2015**, 346 (15), 278-283
Pt@UiO-66[S47]	Pt	terephthalate	~0.12 mmol·g^{-1}·h^{-1}	*Chem. Commun*. **2014**, 50 (53), 7063-7066
CdS + RGO@UiO-66[S48]	RGO	terephthalate	~2.1 mmol g^{-1}·h^{-1}	*Chem. Commun*. **2014**, 50 (62), 8533-8535
[FeFe]@ZrPF[S49]	$[Fe_2S_2]$	porphyrin-based carboxylate ligand	~0.29 mmol g^{-1}·h^{-1}	*Chem. Commun*. **2014**, 50 (72), 10390-10393
Pt/NH_2-MIL-101[S50]	Pt	2-amino-terephthalic acid	~0.58 mmol·g^{-1}·h^{-1}	*Chem. Commun*. **2014**, 50 (79), 11645-11648
UiO-66-[FeFe](dcbdt)$(CO)_6$[S51]	[FeFe](bdt)$(CO)_6$	terephthalate	0.26 mmol g^{-1}·h^{-1}	*J. Am. Chem. Soc*. **2013**, 135 (45), 16997-17003
MOF-253-Pt[S52]	Pt	2,2′-bipyridine-5,5′-dicarboxylic acid	~0.1-0.2 mmol·g^{-1}·h^{-1}	*Energy Environ. Sci*. **2013**, 6 (11), 3229-3234
CdS/MIL-101[S53]	Pt	terephthalic acid	14.1 mmol·g_{CdS}^{-1}·h^{-1}	*Chem. Commun*. **2013**, 49 (60), 6761-6763
Pt/Ti-MOF-NH_2[S54]	Pt	2-aminoterephthalic acid	~0.52 mmol·g^{-1}·h^{-1}	*Catal. Sci. Technol*. **2013**, 3 (8), 2092-2097
Pt@MOF[S55]	Pt	H_2bptc+$[Ir(ppy)_2(bpy)]^+$- derived dicarboxylate ligands	~14.87-30.99 mmol g_{Pt}^{-1}·h^{-1}	*J. Am. Chem. Soc*. **2012**, 134 (17), 7211-7214
Al-PMOF[S56]	Pt	porphyrin-based carboxylate ligand	~0.2 mmol·g^{-1}·h^{-1}	*Angew. Chem. Int. Ed*. **2012**, 51 (30), 7440-7444
Pt/Ti-MOF-NH_2[S57]	Pt	2-aminoterephthalic acid	0.37 mmol·g^{-1}·h^{-1}	*J. Phys. Chem. C*. **2012**, 116 (39), 20848-20853
Pt@UiO-66-NH_2[S58]	Pt	2-aminoterephthalic acid	~4.2 mmol g^{-1}·h^{-1}	*Chem. Eur. J*. **2010**, 16 (36), 11133-11138
Section 4: MOFs for photocatalytic H_2 production				
MOF and Cu^I-based materials	Metal Node	Linker	Activity	Reference
$[Cu_4(DNP)(SCN)Cl_4]_n$[S59]	Cu	2,6-bis(1,8-naphthyridine-2-yl)pyridine	~0.03 mmol g^{-1} h^{-1}	*Z. Anorg. Allg. Chem*. **2019,** 8 (645), 623-630
Cu-I-bpy[S60]	Cu	4,4′-bipyridine	7.09 mmol·g^{-1}·h^{-1}	*Angew. Chem. Int. Ed*. **2017**, 56 (46), 14637-14641
$[Cu^{II}(RSH)(H_2O)]n$[S61]	Cu	rhodamine-based carboxylate linker	7.88 mmol·g^{-1}·h^{-1}	*Angew. Chem. Int. Ed*. ***2016,*** 55 (6), 2073–2077

$[Ni_2(PymS)_4]n$[S62]	Ni	pyrimidine-2-thio	6 mmol·g^{-1}·h^{-1}	*J. Mater. Chem. A*. **2015** , 3 (13), 7163-7169
$Zn_{0.4}(CuGa)_{0.3}Ga_2S_4$[S63]	—	—	~1.03 mmol g^{-1} h^{-1}	*J. Catal.* **2014**, 310, 31-36
$Cu(I/II)/_2$-pzc[S64]	Pt	2-pyrazinecarboxylate	~0.002 mmol g^{-1} h^{-1}	*Inorg. Chim. Acta.* **2011**, 373 (1),137-141
$[Ru_2(p\text{-}BDC)_2]n$[S65]	Ru	1,4-benzene dicarboxylate	~3.58 mmol g^{-1} h^{-1}	*Energy Environ. Sci.* **2009**, 2 (4), 397-400
CuO_x/TiO_2[S66]	—	—	~2.7 mmol g^{-1} h^{-1}	*Catal Lett.* **2009**, 133 (1-2), 97-105
p-type Cu_2O[S67]	—	—	~0.045 mmol g^{-1} h^{-1}	*J. Sol. Energy Mater. Sol. Cells.* **2008**, 92 (9),1071-1076
Cu-MIM	**Cu**	**2-methylimidazole**	**57.64 mmol·g^{-1}·h^{-1}**	**This work**
Cu-EIM	**Cu**	**2-ethylimidazole**	**17.98 mmol·g^{-1}·h^{-1}**	**This work**
Cu-IPIM	**Cu**	**2-isopropylimidazole**	**0.47 mmol·g^{-1}·h^{-1}**	**This work**

Table S2. Elemental analysis of Cu-MIM, Cu-EIM and Cu-IPIM.

	C(%)	N(%)	H(%)
Cu-MIM (Calcd)	33.22	19.37	3.48
Cu-MIM (synthsized)	32.89	19.13	3.35
Cu-MIM (After hydrogen production)	32.63	19.09	3.32
Cu-EIM (Calcd)	37.85	17.66	4.45
Cu-EIM (Synthesied)	37.56	17.41	4.21
Cu-EIM (After hydrogen production)	37.70	17.38	4.20
Cu-IPIM (Calcd)	41.73	16.23	5.22
Cu-IPIM (Synthesied)	41.64	16.09	5.23
Cu-IPIM (After hydrogen production)	41.64	16.24	5.25

Table S3. Structural parameters extracted from the K-edge Cu χ(R) space spectra fitting of Cu-MIM.

	Reduced Chi-square (χ_v^2)	R-factor（%）
Cu-MIM	3254.56	0.0678

amp/ S_{02}	$N_{(Cu\text{-}N\ path)}$	$R_{(Cu\text{-}N\ path)}$ (Å)	$\sigma^2_{(Cu\text{-}N\ path)}$ ($10^{-3}Å^2$)	ΔE0 (eV)
1.21 +/- 0.30	2	1.862±0.031	6.5+/-2.6	6.61+/-1.91
amp/ S_{02}	$N_{(Cu\text{-}C\ path)}$	$R_{(Cu\text{-}C\ path)}$ (Å)	$\sigma^2_{(Cu\text{-}C\ path)}$ ($10^{-3}Å^2$)	ΔE_0 (eV)
1.17+/-0.41	4	2.885±0.048	15.6+/-8.9	4.11+/-1.96

References

[1] Wang, Y.; He, C. -T.; Liu, Y. -J.; Zhao, T.; -Q.; Lu, X. -M.; W. Zhang, -X.; Zhang, J. -P.; Chen, X. -M. Copper(I) and Silver(I) 2-Methylimidazolates: Extended Isomerism, Isomerization, and Host−Guest Properties. *Inorg. Chem*. **2012**, 51 (8), 4772-4778.

[2] Huang, X. -C.; Zhang, J. -P.; Lin, Y. -Y.; Chen, X. -M. Triple-stranded helices and zigzag chains of copper(I) 2-ethylimidazolate: solvent polarity-induced supramolecular isomerism. *Chem. Commun*. **2005**, 17, 2232-2234.

[3] Su, Y. -J.; Cui, Y. -L.; Wang, Y.; Lin, R. -B.; Zhang, W. -X.; Zhang, J. -P.; Chen, X. -M. Copper(I) 2-Isopropylimidazolate: Supramolecular Isomerism, Isomerization, and Luminescent Properties. *Cryst. Growth Des*. **2015**, 15 (4), 1735-1739.

[4] Hohenberg, P.; Kohn, W., Inhomogeneous Electron Gas. *Phys. Rev*. **1964**, 136, B864-B871.

[5] Kresse, G.; Furthmüller, J., Efficient Iterative Schemes for ab initio Total-Energy Calculations Using A Plane-Wave Basis Set. *Phys. Rev. B*. **1996**, 54, 11169-11186.

[6] Blöchl, P. E., Projector Augmented-Wave Method. *Phys. Rev. B***. 1994**, 50, 17953-17979.

[7] Perdew, J. P.; Burke, K.; Ernzerhof, M., Generalized Gradient Approximation Made Simple. *Phys. Rev. Lett.* **1996**, 77, 3865-3868.

[8] Henkelman, G.; Uberuaga, B. P.; Jónsson, H., A Climbing Image Nudged Elastic Band Method for Finding Saddle Points and Minimum Energy Paths. *J. Chem. Phys*. **2000**, 113, 9901-9904.

[9] Henkelman, G.; Jónsson, H., Improved Tangent Estimate in the Nudged Elastic Band Method for Finding Minimum Energy Paths and Saddle Points. *J. Chem. Phys*. **2000**, 113, 9978-9985.

[10] Y. Chen, S. Ji, W. Sun, Y. Lei, Q. Wang, A. Li, W. Chen, G. Zhou, Z. Zhang, Y. Wang, L. Zheng, Q. Zhang, L. Gu, X. Han, D. Wang, Y. Li., Engineering the Atomic Interface with Single Platinum Atoms for Enhanced Photocatalytic Hydrogen Production. *Angew. Chem. Int. Ed*. **2020**, 59 (3), 1295-1301.

[11] B.-H. Lee, S. Park, M. Kim, A. K. Sinha, S. C. Lee, E. Jung, W. J. Chang, K.-S. Lee, J. H. Kim, S.-P. Cho, H. Kim, K. T. Nam, T. Hyeon., Reversible and cooperative photoactivation of single-atom Cu/TiO_2 photocatalysts. *Nat. Mater.* **2019**, 18 (6), 620-628.

[12] R. Shi, C. Tian, X. Zhu, C.-Y. Peng, B. Mei, L. He, X.-L. Du, Z. Jiang, Y. Chen, S. Dai., Achieving an exceptionally high loading of isolated cobalt single atoms on a porous carbon matrix for efficient visible-light-driven photocatalytic hydrogen production. *Chem. Sci.* **2019**, *10 (9),* 2585-2591.

[13] W. Zhang, Q. Peng, L. Shi, Q. Yao, X. Wang, A. Yu, Z. Chen, Y. Fu., Merging Single-Atom-Dispersed Iron and Graphitic Carbon Nitride to a Joint Electronic System for High-Efficiency Photocatalytic Hydrogen Evolution. *Small.* **2019**, 15 (50), 1905166.

[14] L. Zeng, C. Dai, B. Liu, C. Xue., Oxygen-assisted stabilization of single-atom Au during photocatalytic hydrogen evolution. *J. Mater. Chem. A*. **2019**, 7 (42), 24217-24211.

[15] S. Qiu, Y. Shen, G. Wei. S. Yao, W/ Xi, M. Shu, R. Si, M. Zhang, J. Zhu, C. An., Carbon dots decorated ultrathin CdS nanosheets enabling in-situ anchored Pt single atoms: A highly efficient solar-driven photocatalyst for hydrogen evolution. *Applied Catalysis B: Environmental.* **2019**, 259 (15), 118036.

[16] T. He, S. Chen, B. Ni, Y. Gong, Z. Wu, L. Song, L. Gu, W. Hu, X. Wang., Zirconium-Porphyrin-Based Metal-Organic Framework Hollow Nanotubes for Immobilization of Noble‐Metal Single Atoms. *Angew. Chem. Int. Ed.* **2018**, 57 (13), 3493-3498.

[17] Q. Zhao, J. Sun, S. Li, C. Huang, W. Yao, W. Chen, T. Zeng, Q. Wu, Q. Xu., Single Nickel Atoms Anchored on Nitrogen-Doped Graphene as a Highly Active Cocatalyst for Photocatalytic H_2 Evolution. *ACS Catal.* **2018**, 8 (12), 11863-11874.

[18] S. Cao, H. Li, T. Tong, H.-C. Chen, A. Yu, J. Yu, H. M. Chen., Single-Atom Engineering of Directional Charge Transfer Channels and Active Sites for Photocatalytic Hydrogen Evolution. *Adv. Funct. Mater.* **2018**, 28 (32), 1802169.

[19] H. Su, W. Che, F. Tang, W. Cheng, X. Zhao, H. Zhang, Q. Liu., Valence Band Engineering via PtII Single-Atom Confinement Realizing Photocatalytic Water Splitting. *J. Phys. Chem. C.* **2018**, 122 (37), 21108-21114.

[20] Y. Cao, D. Wang, Y. Lin, W. Liu, L. Cao, X. Liu, W. Zhang, X. Mou, S. Fang, X. Shen, T. Yao., Single Pt Atom with Highly Vacant d-Orbital for Accelerating Photocatalytic H_2 Evolution. *ACS Appl. Energy Mater*. **2018,** 1 (11), 6082-6088.

[21] W. Liu, L. Cao, W. Cheng, Y. Cao, X. Liu, W. Zhang, X. Mou, L. Jin, X. Zheng, W. Che, Q. Liu, T.Yao, S. Wei., Single-Site Active Cobalt-Based Photocatalyst with a Long Carrier Lifetime for Spontaneous Overall Water Splitting. *Angew. Chem. Int. Ed.* **2017**, 56 (32), 9312-9317.

[22] Y. Cao, S. Chen, Q. Luo, H. Yan, Y. Lin, W. liu, L. Cao, J. Lu, J. Yang, T. Yao, S. Wei., Atomic-Level Insight into Optimizing the Hydrogen Evolution Pathway over a Co_1-N_4 Single-Site Photocatalyst. *Angew. Chem. Int. Ed.* **2017**, 56 (40), 12191-12196.

[23] X. L. Du, X. L. Wang, Y. H. Li, Y. L. Wang, J. J. Zhao, L. J. Fang, L. R. Zheng, H. Tong, H. G. Yang., Isolation of single Pt atoms in a silver cluster: forming highly efficient silver-based cocatalysts for photocatalytic hydrogen evolution. *Chem. Commun.* **2017**, 53 (68), 9402-9405.

[24] Q. Zhao, W. Yao, C. Huang, Q. Wu, Q. Xu., Effective and Durable Co Single Atomic Cocatalysts for Photocatalytic Hydrogen Production. *ACS Appl. Mater. Interfaces.* **2017**, 9 (49), 42734-42741.

[25] Y. Sui, S. Liu, T. Li, Q. Liu, T. Jiang, Y. Guo, J-L. Luo., Atomically dispersed Pt on specific TiO_2 facets for photocatalytic H_2 evolution. *J. Catal.* **2017**, *353*, 250-255.

[26] X. Li, W. Bi, L. Zhang, S. Tao, W. Chu, Q. Zhang, Y. Luo, C. Wu, Y. Xie., Single-Atom Pt as Co-Catalyst for Enhanced Photocatalytic H_2 Evolution. *Adv. Mater.* **2016**, 28 (12), 2427-2431.

[27] Q. Zuo, T. Liu, C. Chen, Y. Ji, X. Gong, Y. Mai, Y. Zhou., Ultrathin Metal-Organic Framework Nanosheets with Ultrahigh Loading of Single Pt Atoms for Efficient Visible-Light-Driven Photocatalytic H_2 Evolution. *Angew. Chem. Int. Ed.* **2019**, 58 (30), 10198-10203.

[28] J. Ran, H. Zhang, J. Qu, B. Xia, X. Zhang, S. Chen, L. Song, L. Jing, R. Zheng, S.-Z. Qiao., Atomically Dispersed Single Co Sites in Zeolitic Imidazole Frameworks Promoting High-Efficiency Visible-Light-Driven Hydrogen Production. *Chem. Eur. J.* **2019**, 25 (41), 9670-9677.

[29] J. Li, H. Huang, P. Liu, Z. Song, D. Mei, Y. Tang, X. Wang, C. Zhong., Metal-organic framework encapsulated single-atom Pt catalysts for efficient photocatalytic hydrogen evolution. *J. Catal.* **2019**, *375*, 351-360.

[30] X. Fang, Q. Shang, Y. Luo, H.-L. Jiang., Single Pt Atoms Confined into a Metal–Organic Framework for Efficient Photocatalysis. *Adv. Mater*. **2018**, 30 (7), 1705112.

[31] T. Banerjee, F. Haase, G. Savasci, K. Gottschling, C. Ochsenfeld, B. V. Lotsch., Single-Site Photocatalytic H2 Evolution from Covalent Organic Frameworks with Molecular Cobaloxime Co-Catalysts. *J. Am. Chem. Soc.* **2017**, 139 (45), 16228-16234.

[32] J. Ran, J. Qu, H. Zhang, T. Wen, H. Wang, S. Chen, L. Song, X. Zhang, L. Jing, R. Zheng, S.-Z. Qiao., 2D Metal Organic Framework Nanosheet: A Universal Platform Promoting Highly Efficient Visible-Light-Induced Hydrogen Production. *Adv. Energy Mater.* **2019**, 9 (11), 1803402.

[33] Zhang, F. M.; Sheng, J. L.; Yang, Z. D.; Sun, X. J.; Tang, H. L.; Lu, M.; Dong, H.; Shen, F. C.; Liu, J.; Lan, Y. Q. Rational Design of MOF/COF Hybrid Materials for Photocatalytic H_2 Evolution in the Presence of Sacrificial Electron Donors. *Angew. Chem. Int. Ed*. **2018**, 57 (37), 12106-12110.

[34] F. Leng, H. Liu, M. Ding, Q.-P. Lin, H.-L. Jiang., Boosting Photocatalytic Hydrogen Production of Porphyrinic MOFs: The Metal Location in Metalloporphyrin Matters. *ACS Catal.* **2018**, *8 (5)*, 4583-4590.

[35] M. Lan, R.-M. Guo, Y. Dou, J. Zhou, A. Zhou, J.-R. Li., Fabrication of porous Pt-doping heterojunctions by using bimetallic MOF template for photocatalytic hydrogen generation. *Nano Energy.* **2017**, *33*, 238-246.

[36] Chen, Y.-F.; Tan, L.-L.; Liu, J.-M.; Qin, S.; Xie, Z.-Q.; Huang, J.-F.; Xu, Y.-W.; Xiao, L.-M.; Su, C.-Y. Calix[4]arene based dye-sensitized Pt@UiO-66-NH_2 metal-organic framework for efficient visible-light photocatalytic hydrogen production. *Appl. Catal. B-Environ*. **2017**, 206 (5), 426-433.

[37] Wu, Z.-L.; Wang, C.-H.; Zhao, B.; Dong, J.; Lu, F.; Wang, W.-H.; Wang, W.-C.; Wu, G.-J.; Cui, J.-Z.; Cheng, P. A Semi-Conductive Copper–Organic Framework with Two Types of Photocatalytic Activity. *Angew. Chem. Int. Ed.* **2016**, 55 (16), 4938-4942.

[38] J.-D. Xiao, Q. Shang, Y. Xiong, Q. Zhang, Y. Luo, S.-H. Yu, H.-L. Jiang, Boosting Photocatalytic Hydrogen Production of a Metal–Organic Framework Decorated with Platinum Nanoparticles: The Platinum Location Matters. *Angew. Chem. Int. Ed.* **2016**, 55 (32), 9389-9393.

[39] Zhen, W.; Ma, J.; Lu, G., Small-sized Ni(1 1 1) particles in metal-organic frameworks with low over-potential for visible photocatalytic hydrogen generation. Appl. *Catal. B-Environ*. **2016**, 190 (5), 12-25.

[40] Zhang, Z.-M.; Zhang, T.; Wang, C.; Lin, Z.; Long, L.-S.; Lin, W.-B., Photosensitizing Metal−Organic Framework Enabling Visible-Light Driven Proton Reduction by a Wells-Dawson-Type Polyoxometalate. *J. Am. Chem. Soc*. **2015**, 137 (9), 3197-3200.

[41] Nasalevich, M. A.; Becker, R.; Ramos-Fernandez, E. V.; Castellanos, S.; Veber, S. L.; Fedin, M. V.; Kapteijn, F.; Reek, J. N. H.; Vlugt, J. I. van der; Gascon, *J*., Co@NH_2-MIL-125(Ti): cobaloxime-derived metal-organic framework-based composite for light driven H_2 production. *Energy Environ. Sci*. **2015**, 8 (1), 364-375.

[42] Hou, C.-C.; Li, T.-T.; Cao, S.; Chen, Y.; Fu, W.-F., Incorporation of a $[Ru(dcbpy)(bpy)_2]^{2+}$ photosensitizer and a $Pt(dcbpy)Cl_2$ catalyst into metal–organic frameworks for photocatalytic hydrogen evolution from aqueous solution. *J. Mater. Chem. A*. **2015**, 3 (19), 10386-10394.

[43] Balapanuru, J.; Chiu, G.; Su, C.; Zhou, N.; Hai, Z.; Xu, Q.-H.; Loh, K. P., Photoactive PDI−Cobalt Complex Immobilized on Reduced Graphene Oxide for Photoelectrochemical Water Splitting. *ACS Appl. Mater. Interfaces* **2015**, 7 (1), 880-886.

[44] Wang, R.; Gu, L.; Zhou, J.; Liu, X.; Teng, F.; Li, C.; Shen, Y.; Yuan, Y., Quasi-Polymeric Metal–Organic Framework UiO-66/g-C_3N_4 Heterojunctions for Enhanced Photocatalytic Hydrogen Evolution under Visible Light Irradiation. *Adv. Mater. Interfaces*. **2015**, 2 (10), 1500037.

[45] Yuan, Y.-P.; Yin, L.-S.; Cao, S.-W.; Xu, G.-S.; Li, C.-H.; Xue, C., Improving photocatalytic hydrogen production of metal–organic framework UiO-66 octahedrons by dye-sensitization. *Appl. Catal. B-Environ*. **2015**, 168-169, 572-576.

[46] Zhou, J.-J.; Wang, R.; Liu, X.-L.; Peng, F.-M.; Lia, C.-H.; Teng, F.; Yuan, Y.-P., In situ growth of CdS nanoparticles on UiO-66 metal-organic framework octahedrons for enhanced photocatalytic hydrogen production under visible light irradiation. *Appl. Surf. Sci*. **2015**, 346 (15), 278-283.

[47] He, J.; Wang, J.; Chen, Y.; Zhang, J.; Duan, D.; Wang, Y.; Yan, Z., A dye-sensitized Pt@UiO-66(Zr) metal–organic framework for visible-light photocatalytic hydrogen production. *Chem. Commun*. **2014**, 50 (53), 7063-7066.

[48] R. Lin, L. Shen, Z. Ren, W. Wu, Y. Tan, H. Fu, J. Zhang, L. Wu., Enhanced photocatalytic hydrogen production activity via dual modification of MOF and reduced graphene oxide on CdS. *Chem. Commun*. **2014**, 50 (62), 8533-8535.

[49] Sasan, K.; Lin, Q.-P.; Mao, C.-Y.; Feng, P.-Y., Incorporation of iron hydrogenase active sites into a highly stable metal–organic framework for photocatalytic hydrogen generation. *Chem. Commun*. **2014**, 50 (72), 10390-10393.

[50] Wen, M.; Mori, K.; Kamegawa, T.; Yamashita, H., Amine-functionalized MIL-101(Cr) with imbedded platinum nanoparticles as a durable photocatalyst for hydrogen production from water. *Chem. Commun*. **2014**, 50 (79), 11645-11648.

[51] Pullen, S.; Fei, H.; Orthaber, A.; Cohen, S. M.; Ott, S., Enhanced Photochemical Hydrogen Production by a Molecular Diiron Catalyst Incorporated into a Metal−Organic Framework. *J. Am. Chem. Soc*. **2013**, 135 (45), 16997-17003.

[52] Zhou, T.; Du, Y.; Borgna, A.; Hong, J.; Wang, Y.; Han, J.; Zhang, W.; Xu, R., Post-synthesis modification of a metal–organic framework to construct a bifunctional photocatalyst for hydrogen production. *Energy Environ. Sci*. **2013**, 6 (11), 3229-3234.

[53] He, J.; Yan, Z.; Wang, J.; Xie, J.; Jiang, L.; Shi, Y.; Yuan, F.; Yu, F.; Sun, Y., Significantly enhanced photocatalytic hydrogen evolution under visible light over CdS embedded on metal–organic frameworks. *Chem. Commun*. **2013**, 49 (60), 6761-6763.

[54] Toyao, T.; Saito, M.; Horiuchi, Y.; Mochizuki, K.; Iwata, M.; Higashimurab, H.; Matsuoka, M., Efficient hydrogen production and photocatalytic reduction of nitrobenzene over a visible-light-responsive metal–organic framework photocatalyst. *Catal. Sci. Technol*. **2013**, 3 (8), 2092-2097.

[55] Wang, C.; deKrafft, K. E.; Lin, W., Pt Nanoparticles@Photoactive Metal−Organic Frameworks: Efficient Hydrogen Evolution via Synergistic Photoexcitation and Electron Injection. *J. Am. Chem. Soc*. **2012**, 134 (17), 7211-7214.

[56] Fateeva, A.; Chater, P. A.; Ireland, C. P.; Tahir, A. A.; Khimyak, Y. Z.; Wiper, P. V.; Darwent, J. R.; Rosseinsky, M. J., A Water-Stable Porphyrin-Based Metal-Organic Framework Active for Visible-Light Photocatalysis. *Angew. Chem. Int. Ed*. **2012**, 51 (30), 7440-7444.

[57] Horiuchi, Y.; Toyao, T.; Saito, M.; Mochizuki, K.; Iwata, M.; Higashimura, H.; Anpo, M.; Matsuoka, M., Visible-Light-Promoted Photocatalytic Hydrogen Production by Using an Amino-Functionalized Ti(IV) Metal−Organic Framework. *J. Phys. Chem. C.* **2012**, 116 (39), 20848-20853.

[58] Silva, C. G.; Luz, I.; Xamena, F. X. L.; Corma, A.; García, H., Water Stable Zr–Benzenedicarboxylate Metal–Organic Frameworks as Photocatalysts for Hydrogen Generation. *Chem. Eur. J.* **2010**, 16 (36), 11133-11138.

[59] Li, L.; Huang, L.; Liu, Z-Y.; Zhao, X-J.; Yang, E-C., A Polypyridyl-Based Layered Complex as Dual-Functional Co-catalyst for Photo-Driven Organic Dyes Degradation and Water Splitting. *Z. Anorg. Allg. Chem.* **2019,** 8 (645), 623-630.

[60] Shi, D.; Zheng, R.; Sun, M. -J.; Cao, X.; Sun, C.; Cui, C. -J.; Liu, C. -S.; Zhao, J.; Du, M. Semiconductive Copper(I)–Organic Frameworks for Efficient LightDriven Hydrogen Generation Without Additional Photosensitizers and Cocatalysts. *Angew. Chem. Int. Ed*. **2017**, 56 (46), 14637-14641.

[61] Dong, X.-Y.; Zhang, M.; Pei, R.-B.; Wang, Q.; Wei, D.-H.; Zang, S.-Q.; Fan, Y.-T.; Mak, T. C. W., A Crystalline Copper(II) Coordination Polymer for the Efficient Visible-Light-Driven Generation of Hydrogen. *Angew. Chem. Int. Ed*. **2016**, 55 (6), 2073–2077.

[62] Feng, Y.; Chen, C.; Liu, Z.; Fei, B.; Lin, P.; Li, Q.; Sun, S.; Du, S., Application of a Ni mercaptopyrimidine MOF as highly efficient catalyst for sunlight-driven hydrogen generation. *J. Mater. Chem. A*. **2015** , 3 (13), 7163-7169.

[63] Hiroshi, K.; Akihiko, K., Cosubstituting effects of copper(I) and gallium(III) for $ZnGa_2S_4$ with defect chalcopyrite structure on photocatalytic activity for hydrogen evolution. *J. Catal*. **2014**, 310, 31-36.

[64] Sun, X.; You, W., Cheng, H.; Zhang, F.; Meng, B.; Zhang, L., A new host 3D copper(I/II)-pyrazinecarboxylate framework intercalated with Keggin polyoxotungstates. *Inorg. Chim. Acta.* **2011**, 373 (1),137-141.

[65] Kataoka, Y.; Sato, K.; Miyazaki, Y.; Masuda, K.; Tanaka, H.; Naito, S.; Mori, W., Photocatalytic hydrogen production from water using porous material $[Ru_2(p\text{-}BDC)_2]_n$. *Energy Environ. Sci.* **2009**, 2 (4), 397-400.

[66] Wu, Y.; Lu, G.; Li, S., The Role of Cu(I) Species for Photocatalytic Hydrogen Generation Over CuO_x/TiO_2. *Catal Lett.* **2009***,* 133 (1-2), 97-105.

[67] Hu, C-C.; Nian, J-N.; Teng, H., Electrodeposited p-type Cu_2O as photocatalyst for H_2 evolution from water reduction in the presence of WO_3. *J. Sol. Energy Mater. Sol. Cells.* **2008**, 92 (9),1071-1076.